Small

NANO · MICRO small
www.small-journal.com

RESEARCH ARTICLE

Flexible Spin Orientation Optimized Lower-Density Zero Thermal Expansion in the Sc-Based Kagome Magnets

Haowei Zhou[1] | Yanming Sun[1] | Yili Cao[1] | Sergii Khmelevskyi[2] | Tieqiao Zhang[3] | Yaozu Shen[1] | Zhao Pan[4] | Kun Lin[1] | Maxim Avdeev[5,6] | Xianran Xing[1]

[1]Institute of Solid State Chemistry, State Key Laboratory for Advanced Metals and Materials, University of Science and Technology Beijing, Beijing, P. R. China | [2]Vienna Scientific Cluster Research Center, Technical University of Vienna, Vienna, Austria | [3]School of Materials Science and Engineering, Tsinghua University, Beijing, P. R. China | [4]Beijing National Laboratory for Condensed Matter Physics, Institute of Physics, Chinese Academy of Sciences, Beijing, P. R. China | [5]Australian Nuclear Science and Technology Organisation, Lucas Heights, New South Wales, Australia | [6]School of Chemistry, The University of Sydney, Sydney, New South Wales, Australia

Correspondence: Yili Cao (yilicao@ustb.edu.cn) | Xianran Xing (xing@ustb.edu.cn)

Received: 4 October 2025 | **Revised:** 14 January 2026 | **Accepted:** 14 January 2026

Keywords: kagome metal | low density | magnetic structure | zero thermal expansion

ABSTRACT

A variety of lightweight, high-precision engineering approaches are urgently required to decrease the density of metallic components exhibiting zero thermal expansion (ZTE). Scandium, the lightest rare-earth element, plays a unique role in the emergent quantum orders of Kagome metals. Here, we report the controlled design of interplanar magnetic order and thermal expansion in a family of Kagome (Sc,Ti)Fe_2 compounds. Optimizing the Sc-Ti-Fe ternary composition enables ZTE behavior up to room temperature ($\alpha_l = +0.18 \times 10^{-6}$ K^{-1}, 112–300 K) in $Sc_{0.4}Ti_{0.6}Fe_{2.4}$, together with a relatively low density of 6.56 g/cm^3, which is much smaller than that of the documented ZTE alloys. Scanning transmission electron microscopy, Mössbauer spectroscopy, neutron powder diffraction, and theoretical calculations reveal that the extra positive magnetic exchange interactions of antisite Fe stabilize strong in-plane ferromagnetic order and suppresses spin reorientation from in-plane to out-of-plane upon heating. Local magnetic moments of Fe(2*a*) and Fe(6*h*) sites decrease successively over a wider temperature range, thus yielding such ZTE performance. The nearly isotropic ZTE of the ingot indicates its practical potential for advanced functional applications.

1 | Introduction

Zero thermal expansion (ZTE) metals that exhibit neither expansion nor contraction with temperature have been one of the essential components for advanced modern devices [1–3]. Decreasing the density of ZTE metals is demanded for many lightweight applications, particularly in satellites and the aerospace industry [4–7]. To date, most of the metallic ZTEs have been rooted in diverse magnetic transitions, including ferromagnetic-paramagnetic (FM-PM) in $Fe_{65}Ni_{35}$ [8], $(Zr_{0.65}Nb_{0.35})_{0.95}Fe_{0.05}Fe_2$ [9], and $LaFe_{10.6}Co_{1.0}Si_{1.4}$ [10], antiferromagnetic-paramagnetic (AFM-PM) in $Mn_3Cu_{0.5}Ge_{0.5}N$ [11], ferromagnetic-antiferromagnetic (FM-AFM) in $Hf_{0.86}Ta_{0.14}Fe_2$ [12], ferrimagnetic-paramagnetic (FIM-PM) in $Ho_2Fe_{16}Co$ [13] and $TbCo_{1.9}Fe_{0.1}$ [14]. However, most ZTE systems more or less consist of various heavy elements (e.g., Tb: 8.23 g/cm^3; Hf: 13.31 g/cm^3), and thus yield higher densities, such as 9.76 g/cm^3 in $TbCo_{1.9}Fe_{0.1}$, and even 10.1 g/cm^3 in $Hf_{0.8}Nb_{0.2}Fe_{2.5}$ [15]. Moreover, practical applications of metals also require isotropic ZTE at the macroscale, yet is limited to very few cubic phases [16–20].

Haowei Zhou and Yanming Sun contributed equally to this work.

Kagome lattice refers to 2D corner-sharing triangles, which is a geometrically frustrated network [21–24]. The strong electronic-geometry correlation provides an excellent platform for discovering quantum orders and related physical properties, such as the coexistence of a charge density wave (CDW) and superconductivity [25, 26], anomalous Hall effects [27, 28], and negative thermal expansion (NTE) [29–31]. To decrease the density, scandium (Sc), as the smallest atomic radius (1.6641 Å) and the lowest density (2.985 g/cm^3) among all rare earth elements, not only contributes a distinct spatial effect for tuning order parameters of kagome metals such as CDW in ScV_6Sn_6 [32, 33], but also lowers the density of the products.

Laves phase intermetallic compounds AB_2, as a typical kagome system, show the flexible chemical regulations of magnetic orders and thermal expansion [34–37]. One of the candidates is the hexagonal $ScFe_2$ compound (Space group: $P6_3/mmc$). Titanium (Ti, 4.51 g/cm^3) substitutions for Sc in $ScFe_2$ can induce a local magnetic change along the *c* direction and thus the NTE or ZTE [38–40]. Nevertheless, such thermal expansion anomaly occurs below room temperature, and the precise relationship between thermal expansion and magnetic structures, as well as how it can be controlled, remains unclear. Is there any other hidden orders in the magnetic transition, such as antiferromagnetism and spin reorientation dominating the NTE or ZTE?

Herein, we design a series of $(Sc,Ti)Fe_{2+y}$ compounds with trace Fe doping to study the magnetic order and thermal expansion. It was clearly revealed that the NTE behavior in $(Sc,Ti)Fe_2$ involves a spin reorientation from in-plane to out-of-plane FM ordering. Off-stoichiometric Fe introduces antisite Fe(*4f*) atoms, which stabilize strong FM ordering. Consequently, a room temperature ZTE $Sc_{0.4}Ti_{0.6}Fe_{2.4}$ was found, ($\alpha_V = +1.93 \times 10^{-6}$ K^{-1}, 5–300 K) with a density of 6.56 g/cm^3. The good metallicity and nearly isotropic ZTE in the ingot make it promising for applications.

2 | Result and Discussion

All Laves phases $(Sc,Ti)Fe_2$ crystallize in a hexagonal $P6_3/mmc$ structure. Little excess Fe can be introduced into the matrix and maintains such hexagonal symmetry, offering composition freedom to optimize the magnetic orders and thermal expansion across the Sc-Ti-Fe ternary phase diagram (Figure 1a). Herein, we prepared the $Sc_{0.35}Ti_{0.65}Fe_{2+y}$, $Sc_{0.4}Ti_{0.6}Fe_{2+y}$, $Sc_{0.45}Ti_{0.55}Fe_{2+y}$, and $Sc_{0.5}Ti_{0.5}Fe_{2+y}$ series, among which the $(Sc_{0.4}Ti_{0.6})Fe_{2+y}$ was selected in detailed investigation (Figures S1and S3). Synchrotron X-ray powder diffraction (SXRD) confirms that the sample adopts a hexagonal structure at room temperature (Figure 1b,c), in which the hexagonal structure has two equivalent 2D kagome planes along the (001) crystal plane. The inset of Figure 1c shows that the peaks (100) and (002) shift to the high angle in comparison with $Sc_{0.4}Ti_{0.6}Fe_2$ (denoted as $y = 0$). X-ray energy dispersive spectroscopy (EDS) elemental analysis shows homogeneous elemental distribution with composition of Sc: Ti: Fe = 0.40: 0.59: 2.40, consistent with the designed composition (Figure 1d). High-angle annular dark-field (HAADF) images along the [100] zone axis show the atomic stacking, including the kagome Fe(6 *h*) layers and other types of atoms between the layers (Figure 1e; Figure S2). Elemental mapping in Figure 1f shows that Sc and Ti all evenly occupy the 4*f* sites. The Fe mapping indicates that, besides the parent Fe(2*a*) and Fe(6 *h*) sites, Fe atoms also occupy the Sc/Ti(4*f*) sites, as highlighted by the yellow arrow. Moreover, intensity analysis demonstrates that the spectrum from the red region contains an additional peak corresponding to the Sc/Ti(4*f*) site, absent in the gray region, confirming that non-stoichiometric Fe atoms preferentially occupy the 4f antisite.

The macroscopic linear thermal expansions of $Sc_{0.4}Ti_{0.6}Fe_{2+y}$ (y = 0, 0.2, 0.4, and 0.8) compounds were measured along the *z* direction in Figure 2a. The NTE was observed from 112–205 K in $Sc_{0.4}Ti_{0.6}Fe_2$ ($\alpha_l = -7.83 \times 10^{-6}$ K^{-1}) as reported before [38]. With increasing Fe content, the NTE behavior is gradually suppressed. In the temperature window of 112–300 K, the $Sc_{0.4}Ti_{0.6}Fe_{2.4}$ (y = 0.4) achieves near room-temperature ZTE with a coefficient of thermal expansion (CTE) ($\alpha_l = +0.18 \times 10^{-6}$ K^{-1}). Interestingly, although the $y = 0.4$ composition has hexagonal symmetry, the ingot exhibits similar ZTE behavior along the three mutually perpendicular directions due to its microstructural features [41] ($\alpha_x = +0.53 \times 10^{-6}$ K^{-1}, $\alpha_y = +0.62 \times 10^{-6}$ K^{-1}, $\alpha_z = +0.18 \times 10^{-6}$ K^{-1}; 112–300 K) (Figures 2b; S5). Such ZTE was also achieved in other Sc-Ti-Fe ternary samples, e.g. $Sc_{0.5}Ti_{0.5}Fe_{2.15}$: $\alpha_l = -0.32 \times 10^{-6}$ K^{-1}, 112–263 K; $Sc_{0.45}Ti_{0.55}Fe_{2.3}$: $\alpha_l = +0.57 \times 10^{-6}$ K^{-1}, 112–273 K; $Sc_{0.35}Ti_{0.65}Fe_{2.6}$: $\alpha_l = +0.72 \times 10^{-6}$ K^{-1}, 112–300 K (Figures 2c; S4). 2D contour plots of the temperature-dependence SXRD patterns show a slight shift of the (100) and (002) peaks below 300 K in $y = 0.4$ (Figure 2d). As shown in Figures 2e and S6, the lattice parameter *V* of $Sc_{0.4}Ti_{0.6}Fe_{2.4}$ exhibits almost low thermal expansion over a wide temperature window from 5 to 300 K ($\alpha_V = +1.93 \times 10^{-6}$ K^{-1}). The CTE in the *ab*-plane ($\alpha_a = -0.08 \times 10^{-6}$ K^{-1}, 5–300 K) is negligible and the *c*-axis also shows a small value ($\alpha_c = +2.10 \times 10^{-6}$ K^{-1}, 5–300 K) (inset in Figure 2e; Table S3), which arises from the hexagonal structure. Moreover, since this series of samples exhibits negligible texture according to our previous study [15, 41], the CTEs along three perpendicular directions are nearly identical, resulting in a nearly isotropic ZTE behavior. Notably, the present $Sc_{0.4}Ti_{0.6}Fe_{2.4}$ also demonstrates the lightest density of 6.56 g/cm^3 among other room temperature ZTE metals (Figure 2f) [8, 9, 14, 15, 41–47], which is 16% smaller than 7.81 g/cm^3 in $Zr_{0.75}Nb_{0.25}Fe_2Co_{0.1}$ (Table S1) [48].

The macroscopic magnetic behaviors of $y = 0$ and $y = 0.4$ were characterized by temperature-dependence of magnetization (*M-T*) curves in Figure 3a. For $y = 0$, the magnetization drops sharply at 122 K, corresponding to the NTE behavior. Fe doping shifts the magnetic transition to higher temperatures and smooths the transition, thereby broadening the anomalous thermal expansion window. Lorentz transmission electron microscopy (LTEM) was used to probe temperature-dependent domain evolution in Figure 3b. For $y = 0$, transverse domain walls along the blue arrows are observed at 115 K. Upon heating, domain rotation results in multiple domain wall orientations coexisting (Figure S7). At 150 K, the domain walls are all arranged along the yellow arrows, nearly orthogonal to those at 115 K, clearly indicating a spin reorientation transition within the NTE temperature range. At higher temperatures, the domains further evolve into densely and regularly aligned parallel walls. However, $y = 0.4$ exhibits prominent domain walls at low temperatures, with no significant reorientation upon heating. The isothermal magnetization (*M–H*) curves also confirm the $y = 0.4$ exhibits FM order at all investigated temperatures and saturation magnetization decreases gradually with temperature (Figures 3c; S8

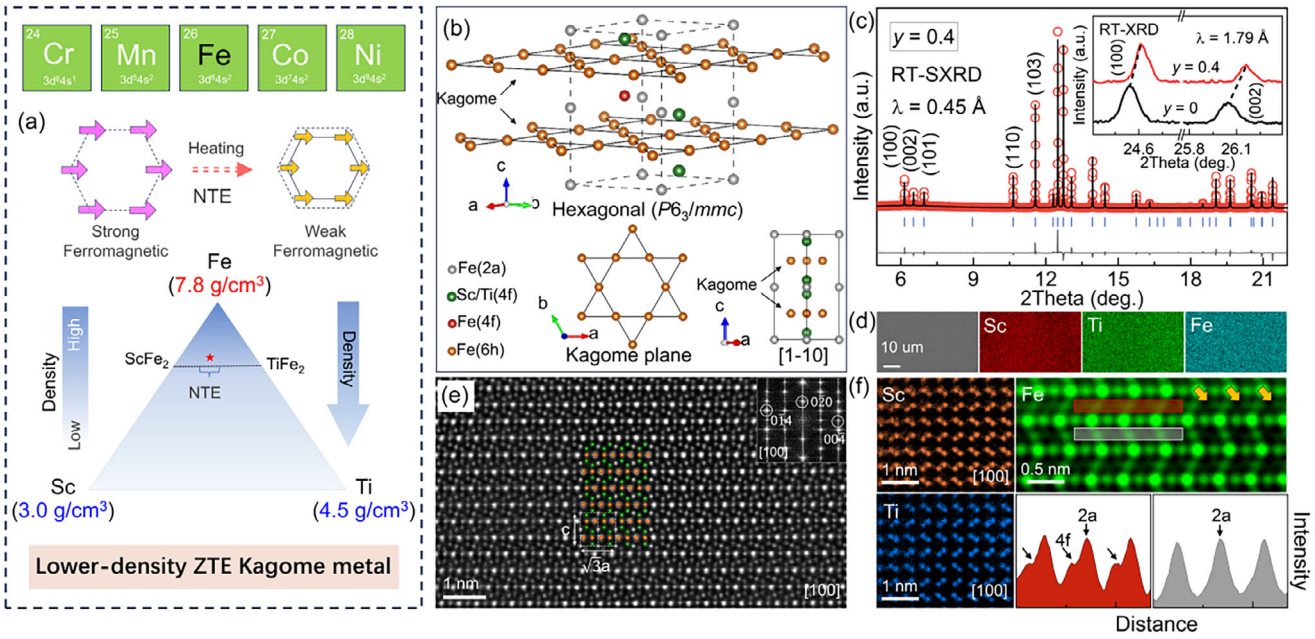

FIGURE 1 | Crystal structure of lower-density ZTE alloys. (a) Schematic diagram for design strategy of developing lower-density ZTE Kagome metal; (b) The kagome hexagonal structure of $(Sc,Ti)Fe_2$; (c) SXRD refinement result of $(Sc_{0.4}Ti_{0.6})Fe_{2+y}$ ($y = 0.4$) at 300 K (the inset shows RT-XRD results for $y = 0$ and 0.4 under Co Kα radiation, respectively); (d) EDS elemental mapping of the $y = 0.4$; (e) HAADF-STEM image along the [100] zone axis of $y = 0.4$ (the inset shows the corresponding FFT profile); (f) Atomically resolved energy-dispersive X-ray spectroscopy (EDXS) mappings (Sc, Ti, and Fe elements) and intensity profiles of Fe atom columns. Colored profiles correspond to the regions with the same color in the Fe pattern.

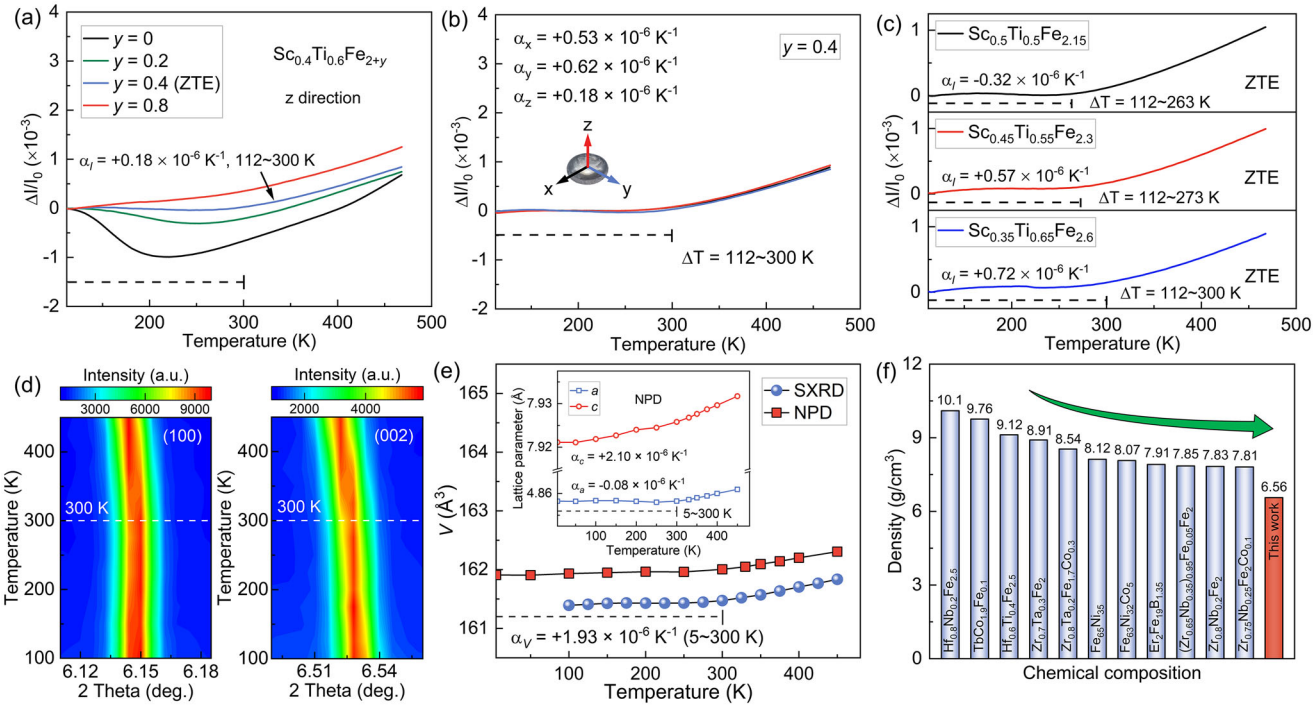

FIGURE 2 | Thermal expansion behaviors of Sc-Ti-Fe alloys. (a) Linear thermal expansion ($\Delta I/I_0$) for $Sc_{0.4}Ti_{0.6}Fe_{2+y}$ ($y = 0$, 0.2, 0.4 and 0.8); (b) Linear thermal expansions of $y = 0.4$, the inset shows the coordinate system of the sample; (c) ZTE alloys $Sc_{0.5}Ti_{0.5}Fe_{2.15}$, $Sc_{0.45}Ti_{0.55}Fe_{2.3}$ and $Sc_{0.35}Ti_{0.65}Fe_{2.6}$; (d) The contour NPD plots of the peaks (100) and (002) in $y = 0.4$; (e) Temperature-dependence of the lattice parameter V of $y = 0.4$ measured by SXRD and NPD (the inset shows temperature-dependence of the lattice parameter (a and c) of $y = 0.4$ measured by NPD); (f) Comparison of densities of various room temperature ZTE alloys.

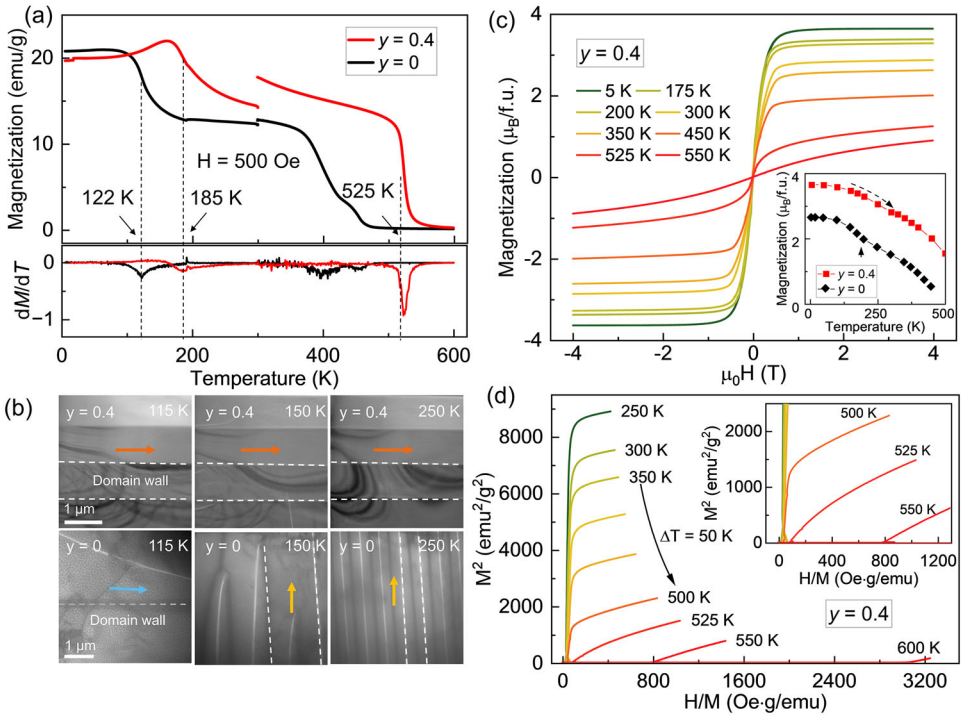

FIGURE 3 | Magnetic properties and domain structure of ZTE alloys. (a) Temperature-dependence of magnetization (M–T) and their differential curves for $y = 0$ and $y = 0.4$ in zero-field cooling (ZFC) under 500 Oe; (b) L-TEM images of the evolution of the magnetic domains of $y = 0$ and $y = 0.4$ as a function of temperature at zero magnetic field. (c) Isothermal magnetization as a function of applied magnetic field (M-H) curves for $y = 0.4$, the inset of the figure is the temperature dependence of saturation magnetization for $y = 0$ and $y = 0.4$; (d) Isothermal Arrot plots of the H/M versus M^2 for $y = 0.4$.

and S9). The isotherm Arrot plots of H/M versus M^2 also show that all the slopes are positive below the Curie temperature (T_C) and spontaneous magnetization disappears near 525 K in $y = 0.4$. This clearly suggests lattice parameters change smoothly as the magnetic phase transition occurs (Figure 3d). These results demonstrate that Fe doping effectively suppresses the spin reorientation, thereby modulating the thermal expansion.

The ^{57}Fe Mössbauer spectra of the non-stoichiometric sample ($y = 0.4$) were collected at 5, 175, and 300 K to probe magnetic splitting of each Fe sublattice (Figure 4a–c). At 5 K, the well-fitted sextets confirm the existence of spontaneous magnetic order. In the hexagonal structure, Fe atoms occupy the Fe(2a) and Fe(6h) crystallographic sites, corresponding to two anisotropies of hyperfine exchange interactions with a ratio of approximately1:3. However, analysis of the $y = 0.4$ sample reveals extra hyperfine interactions originating from a non-stoichiometric Fe(4f) site (Figure 1f). The 5 K fitting curve indicates three hyperfine fields: 20.9 T (22.4%) from the Fe(2a) site, 19.0 T (67.6%) from the Fe(6h) site, and 8.8 T (10%) from the additional Fe(4f) site (Figure 4d). At 175 K, the Fe(6h) site is fitted with three magnetic states, with hyperfine fields of 13.6 T (4.4%), 16.8 T (62.0%), and 23.0 T (1.6%) (Figure 4e), consistent with the magnetization decrease observed in M–T curves. The hyperfine field of the Fe(4f) site decreases slightly, but its ratios of three magnetic sublattices remain similar. By 300 K, the hyperfine fields of all sites decrease markedly: Fe(4f), 5.4 T; Fe(6h) (5.4 T, 10.9 T); and Fe(2a) (14.4 T) in Figure 4f. These results indicate that the magnetic moment of Fe-sublattices decreases with increasing temperature.

To investigate the temperature-dependent magnetic structure of $y = 0.4$, high-resolution neutron powder diffraction (NPD) was performed from 5 to 500 K. It is noteworthy that the contour plots of the NPD patterns show that no additional Bragg peaks were observed within the entire temperature range. The intensity of the (100) peak changes slowly below 300 K, whereas the (002) magnetic peak weakens near 170 K, in agreement with the magnetic transition of M–T curves (Figure 5a). The detailed temperature-dependence of the peak intensity is shown in Figure 5b. The intensity of (002) decreases rapidly near 170 K (Figure 5b), which suggests the moment in the basal plane decreases. Thus, a FM structure with moment lying in the basal plane was determined at 5 K by Rietveld refinement with R_{wp} values of 8.04% (Figures 5c,d; S10 and Table S2). The magnetic moments of all three sublattices align along the same in-plane direction. In contrast, the spin reorientation in $y = 0$ is from in-plane to out of plane upon heating (i.e., basal plane to along the c axis) [38], thus antisite Fe(4f) in $y = 0.4$ stabilizes strong FM order and suppresses spin reorientation. As shown in Figure 5e and Table S3, the moment amplitude decreases significantly—for example, the magnetic moment at the Fe(6h) site reduces from 2.70 (5) μ_B at 5 K to 2.67 (5) at 180 K, and the magnetic moment at the Fe(2a) site increases from 2.81 (9) μ_B at 5 K to 3.26 (9) μ_B at 180 K. The total magnetic moments of Fe sites decrease quickly above 300 K (Tables S4 and S5). The interplay between phonon and magnetism contributions to thermal expansion, leading to the pronounced ZTE behavior, is shown in the inset of Figure 5f. The spontaneous volumetric magnetostriction (ω_S) associated with magnetic ordering increases with the enhancement of FM order, effectively compensating the intrinsic phonon-driven expansion.

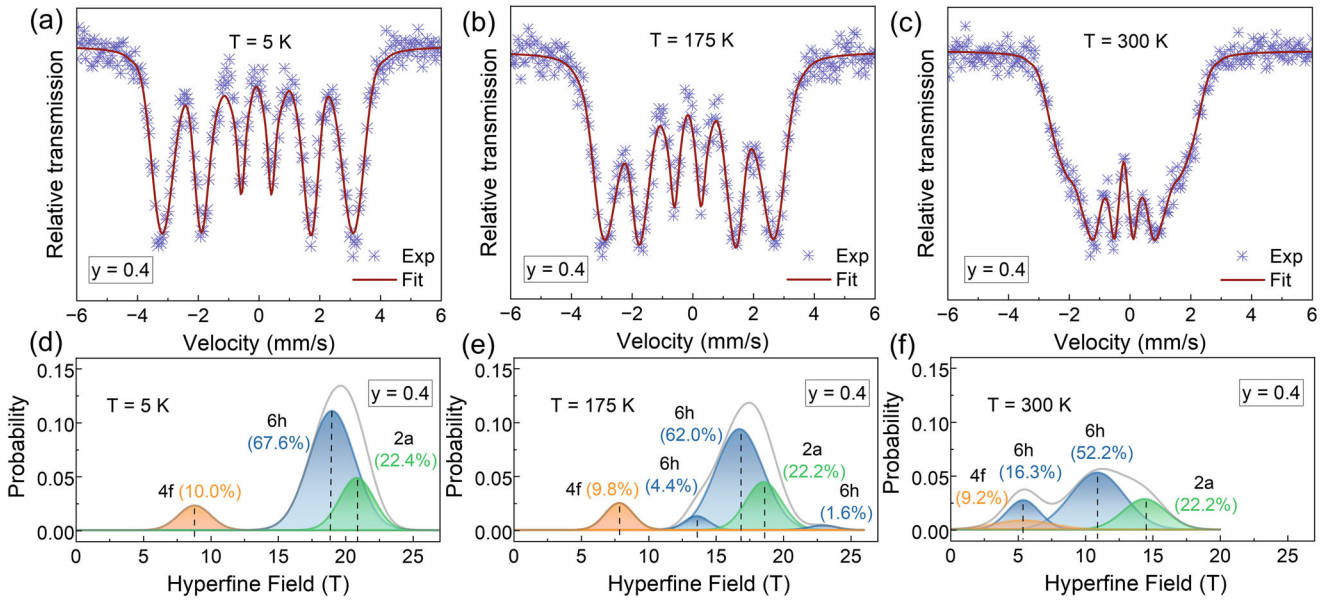

FIGURE 4 | The magnetic hyperfine field distribution. The ^{57}Fe Mössbauer spectrum of $y = 0.4$ measured at (a) 5 K, (b) 175 K, and (c) 300 K, respectively; The hyperfine magnetic field distribution results of $y = 0.4$ at (d) 5 K, (e) 175 K, and (f) 300 K, respectively.

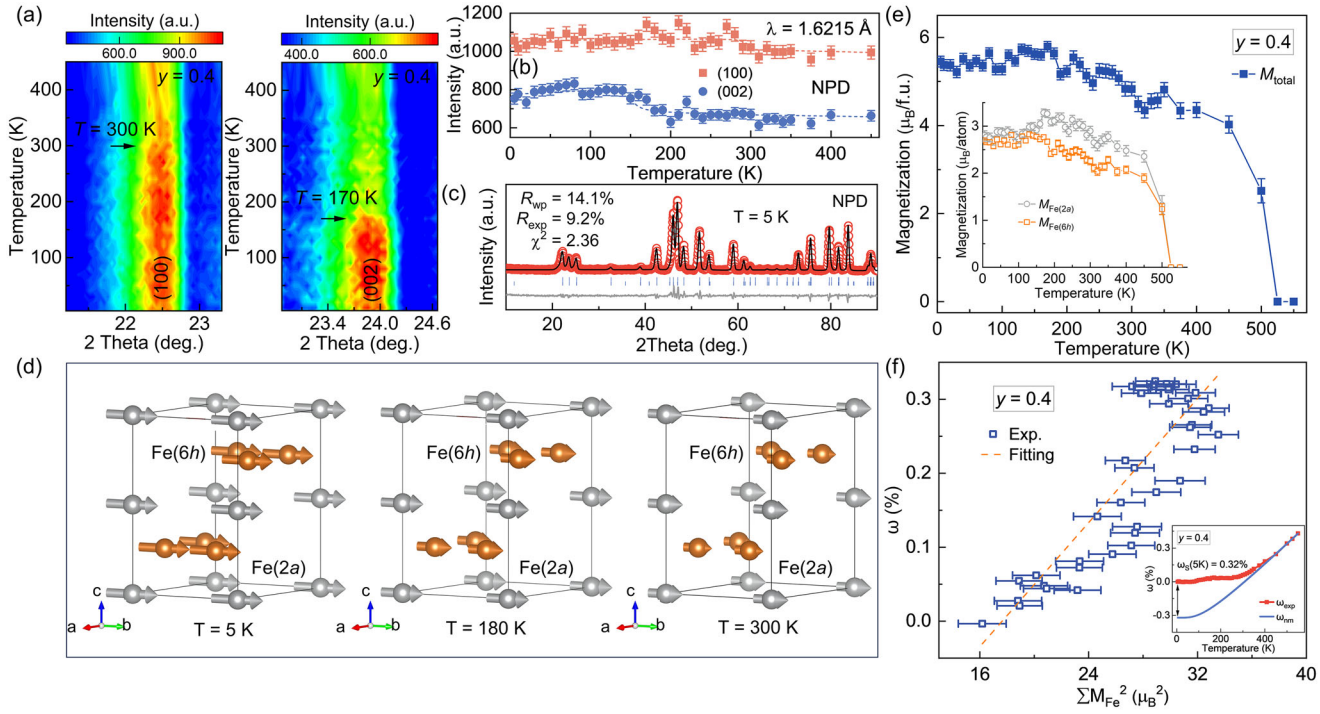

FIGURE 5 | The magnetic structure of Sc-Ti-Fe alloys. (a) Contour plot of NPD patterns and (b) temperature-dependence of peak intensity of peaks (100) and (002) for $y = 0.4$, respectively; (c) Rietveld refinement of NPD patterns at 5 K for $y = 0.4$; (d) The average magnetic structure of $y = 0.4$ at 5, 180, and 300 K, respectively; (e) Temperature dependence of total moments by NPD (the inset shows temperature dependence of the Fe(2*a*) and Fe(6*h*) moment of $y = 0.4$ measured by NPD, respectively); (f) Positive correlation between the magnetic moment of the Fe lattice ($|\Sigma \boldsymbol{M}_{Fe}|$) and the spontaneous volumetric magnetostriction ω_S for $y = 0.4$, the inset shows the calculation of ω_S.

A linear correlation is observed between ω_S and the square of the total magnetic moment. The rate of the change of magnetic moments decreases as excess Fe-doping stabilizes the FM order, the large ω_S maintains up to room temperature, and contributes to such ZTE behavior.

In order to further elucidate the nature of the magnetism in the investigated (Sc,Ti,Fe)Fe_2, we calculate the inter-atomic magnetic interactions of $y = 0.4$ using first principles, as presented in Table 1. We find that at the experimental lattice geometry, the robust FM interactions are present between all Fe sites. The

TABLE 1 | Largest inter-atomic exchange interactions Fe–Fe: J_{ij} (mRy). (AS-antisite).

Compound	State	6*h*-6*h* (1NN)	6*h*-2*a* (1NN)	6*h*-6*h* (2NN)	6*h*-Fe(4*f*) 1NN	6*h*-Fe(4*f*) 2NN	AS-AS 1NN	2*a*-Fe(4*f*) 1NN
$y = 0.4$	FM	1.49	1.19	1.14	1.16	1.17	0.61	1.11

TABLE 2 | The calculated magnetic moments (μ_B) of $Sc_{0.4}Ti_{0.6}Fe_2$ ($y = 0$) and $(Sc_{0.35}Ti_{0.53}Fe_{0.12})Fe_2$ ($y = 0.4$) alloys in the FM ground state and paramagnetic (PM, above T_C) state.

Compound	State	Fe(6*h*)	Fe(2*a*)	Fe(4*f*)	Ti(4*f*)	Sc(4*f*)	Total/f.u.
$y = 0.4$	FM	1.99	1.94	2.83	−0.62	−1.05	3.52
	PM	1.41	1.18	2.95	0	0	—

local moments of Fe(4*f*) sites provide an additional strong FM interaction to the system (see Table 1) and thus make the collinear state more robust. Thus, it can be concluded that the ZTE phenomena observed here are an intrinsic property of the FM phase. As a hypothesis, one speculates that it might occur due to different signs of the single-site anisotropies on different Fe sites that have different temperature dependencies. These temperature dependencies might be rather strong due to the itinerant character of the magnetism on both Fe(2*a*) and Fe(6*h*) sites and thus strongly depend on the electronic structure of the state of the atomic magnetic disorder in the system.

The electronic structure and atomic magnetic moments on different sublattices were also calculated in the framework of the Density Functional Theory [49]. The atomic and total magnetic moments are presented in Table 2. One can see that Fe(6*h*) and Fe(2*a*) sites have a very close value, around 2 μ_B/atom, in the FM state in both compositions, close to what can be seen in pure bcc Fe (2.27 μ_B/atom). However, in the PM state, their values are greatly reduced in both compositions, indicating a strongly itinerant character of the Fe magnetic moments on this site. This situation is similar to those that can be found in classical Invar Fe-Ni [50] and Fe-Pt [16] alloys. It has been argued that such a thermal disorder-induced magnetic moment reduction is a main reason for the onset of the strong negative magnetic contribution to thermal expansion that leads to the ZTE behavior. In contrast, the magnetic moment of Fe on 4*f* sites is found to be strongly localized and state independent, with a magnitude ~3 μ_B/atom that is close to the complete saturation of the Fe moments possible in intermetallic compounds. Note a strong induced spin polarization on Ti and Sc atoms in the FM state that vanishes in the Disordered Local Moments (DLM) state. This polarization is opposite to the direction of Fe moments and contributes significantly to the total magnetization of the alloys, which is not quite a surprise, as Ti and Sc have a *d*-electron band filled with one electron. The total magnetization has been found to be in good agreement with experimental results presented above.

3 | Conclusion

In conclusion, a series of $(Sc,Ti)Fe_{2+y}$ compounds with excess Fe doping were designed, and a room-temperature ZTE composition $Sc_{0.4}Ti_{0.6}Fe_{2.4}$ was found ($\alpha_l = +0.18 \times 10^{-6}$ K^{-1}, 112–300 K) with a density of 6.56 g/cm^3, which is much lower than that previously reported ZTE metals. STEM, Mössbauer spectroscopy, neutron powder diffraction and comprehensive theoretical studies indicate that the antisite Fe atoms in the Sc/Ti 4*f* sites, due to the excess Fe, stabilize the FM order by introducing extra ferromagnetic exchange interactions. Such ZTE was entangled in the decrease of the magnetic moments of Fe(2*a*) and Fe(6*h*) sites with a successive change of interplanar spin orientation upon heating. Along with room-temperature metallic character (electrical resistivity: 1.37×10^{-4} Ω cm; thermal conductivity: 3.04 W m^{-1} K^{-1}) and nearly isotropic behavior, such ZTE metal demonstrates strong potential for future applications.

4 | Experimental Section

4.1 | Materials and Preparations

All Sc–Ti–Fe series samples were synthesized by arc melting, followed by annealing at 1473 K for 72 h and subsequent water quenching to obtain target compounds.

4.2 | Crystal and Magnetic Structure

Powder X-ray diffraction (XRD) was performed using an X-ray diffractometer (SmartLab 9 kw, Rigaku Corporation) with Co Kαradiation (λ = 1.79 Å). Temperature dependence of the synchrotron X-ray diffraction (SXRD) of $Sc_{0.4}Ti_{0.6}Fe_{2.4}$ was collected on the BL02B2 beamline (λ = 0.45033 Å) at SPring-8 (Japan). Temperature dependence of the neutron powder diffraction (NPD) was obtained from the Australian Nuclear Science and Technology Organization (ANSTO) at ECHIDNA (λ = 1.6215 Å). The SXRD and NPD patterns were refined using Fullprof software using the Rietveld method to obtain the lattice parameters and the corresponding crystal and magnetic structures.

4.3 | Structural and Electron Microscopy Characterization

Scanning electron microscopy (SEM) imaging and X-ray energy dispersive spectroscopy (EDS) elemental analysis were obtained

using a GeminiSEM 500 (ZEISS, Germany) scanning electron microscope equipped with an Ultim Max EDS spectrometer (Oxford, UK). Atomic-resolution scanning transmission electron microscopy (STEM) images were obtained using a STEM instrument (Equipment type: JEM-ARM300F2, Accelerating voltage: 80–300 kV, Electron Gun: Cold Field Emission, STEM resolution:53pm, EDS energy resolution: 133 eV). A thin-plate sample (≈100 nm) was prepared from the polycrystalline ingot by focused ion beam milling. The magnetic domain structures were subsequently examined using Lorentz transmission electron microscopy (L-TEM).

4.4 | Dilatometer Thermal Expansion

The linear thermal expansion curves were measured on a thermal expansion meter (NETZSCH DIL402) in the temperature range 112–500 K with a heating rate of 5 K/min using a regular ingot.

4.5 | Magnetization Measurements

Macromagnetism measurements were performed using a physical property measurement system (PPMS, Quantum Design) with a vibrating sample magnetometer (VSM), which has a temperature rate of 6 K/min and a magnetic field sweep rate of 100 Oe/sec. The measurements covered the temperature range of 2–300 K using the low-temperature mode and 300–900 K using the oven option, with the maximum magnetic field of 9 Tesla.

4.6 | Mössbauer Spectrum Measurements

The Mössbauer absorption spectra have been obtained with a rhodium-based ^{57}Co source in standard transmission geometry. The calibration was carried out with an α-Fe foil, and the isomer values are given with reference to α-Fe. A model-independent Hesse-Rübartsch hyperfine magnetic field (H_{hf}) distribution method was used to exactly reflect the microscopic magnetic properties of the Fe moments, where the isomer shift and quadrupole splitting are linearly correlated with Hhf, respectively.

4.7 | Theoretic Calculations

To this end, we used Coherent Potential Approximation (CPA) [51] embedded in the Korringa–Kohn–Rostocker band structure formalism [52]. that allows for calculating the alloys with random atomic distribution of Sc, Ti (and Fe in Fe-excess composition) atoms over 4f-lattice sites. For both alloy compositions, we calculate the magnetic moments for two states-collinear ferromagnetic ordered ground state, where all Fe spin moments oriented in the same direction, and the thermodynamic paramagnetic state (PM) above the Curie temperature with random orientations of the atomic magnetic moments. To model PM state in calculations, we use a conventional magnetic alloy analogy model based on the CPA-so called Disordered Local Moments (DLM) approximation [53]. The inter-atomic magnetic interactions are calculated by Green function-based Magnetic Force Theorem [54] implemented in the framework of KKR method [55]. The exchange coupling constant J_{ij} of the following Heisenberg Hamiltonian:

$$H = -\sum_{i,j\in 6\ h,2a,4f} J_{ij}^{Fe-Fe}\vec{e}_i^{Fe}\vec{e}_j^{Fe}$$

where $\vec{e}_i^{Fe}$ is a unit vector of the Fe magnetic moment directions and indexes are running over all sites of the hexagonal lattice populated by Fe atoms.

Acknowledgements

Haowei Zhou and Yanming Sun contribute equally to this work. This work was supported by the National Natural Science Foundation of China (22090042, 22275015, 22535001, and 52201171), the Fundamental Research Funds for the Central Universities, China (FRF-EYIT-23-03 and FRF-IDRY-23-020). The neutron diffraction experiments were performed in Australian Nuclear Science and Technology Organisation. The synchrotron X-ray diffraction (SXRD) was collected on the BL02B2 beamline at the Spring-8.

Conflicts of Interest

The authors declare no conflicts of interest.

Data Availability Statement

The data that support the findings of this study are available in the supplementary material of this article.

References

1. S. Kulkarni, A. A. Umińska, J. Sanjuán, et al., "Characterization of Dimensional Stability for Materials Used in Ultra-Stable Structures," *Proceedings of Spie—the International Society for Optical Engineering* 11820 (2021): 19.

2. R. Huang, Y. Liu, W. Fan, et al., "Giant Negative Thermal Expansion in $NaZn_{13}$ -Type La(Fe, Si, Co)$_{13}$ Compounds," *Journal of the American Chemical Society* 135 (2013): 11469–11472, https://doi.org/10.1021/ja405161z.

3. J. R. Salvador, F. Guo, T. Hogan, and M. G. Kanatzidis, "Zero Thermal Expansion in YbGaGe due to an Electronic Valence Transition," *Nature* 425 (2003): 702–705, https://doi.org/10.1038/nature02011.

4. Y. Ding, L. Ma, Z. Xu, et al., "Progress on the Use of Satellite Technology for Gravity Exploration," *Geodesy and Geodynamics* 6 (2015): 299–306, https://doi.org/10.1016/j.geog.2015.05.008.

5. Q.-F. Guan, H.-B. Yang, Z.-M. Han, et al., "Lightweight, Tough, and Sustainable Cellulose Nanofiber-Derived Bulk Structural Materials with Low Thermal Expansion Coefficient," *Science Advances* 6 (2020): aaz1114.

6. A. L. Goodwin, M. Calleja, M. J. Conterio, et al., "Colossal Positive and Negative Thermal Expansion in the Framework Material Ag_3 [Co(CN)$_6$]," *Science* 319 (2008): 794–797, https://doi.org/10.1126/science.1151442.

7. F.-X. Hu, B.-G. Shen, J.-R. Sun, Z.-H. Cheng, G.-H. Rao, and X.-X. Zhang, "Influence of Negative Lattice Expansion and Metamagnetic Transition on Magnetic Entropy Change in the Compound $LaFe_{11.4}Si_{1.6}$," *Applied Physics Letters* 78 (2001): 3675–3677, https://doi.org/10.1063/1.1375836.

8. C.-E. Guillaume, "Recherches sur Les Aciers au Nickel. Dilatations Aux Temperatures Elevees; Resistance Electrique," *Comptes Rendus* 125 (1897): 235.

9. Y. Sun, Y. Cao, S. Hu, et al., "Interplanar Ferromagnetism Enhanced Ultrawide Zero Thermal Expansion in Kagome Cubic Intermetallic

(Zr,Nb)Fe_2," *Journal of the American Chemical Society* 145 (2023): 17096–17102, https://doi.org/10.1021/jacs.3c03160.

10. H.-B. Zhou, Z.-B. Yu, F.-X. Hu, et al., "Emergence of Invar Effect with Excellent Mechanical Property by Electronic Structure Modulation in $LaFe_{11.6-x}Co_xSi_{1.4}$ Magnetocaloric Materials," *Acta Materialia* 260 (2023): 119312, https://doi.org/10.1016/j.actamat.2023.119312.

11. S. Iikubo, K. Kodama, K. Takenaka, H. Takagi, and S. Shamoto, "Magnetovolume Effect in $Mn_3Cu_{1-x}Ge_xN$ Related to the Magnetic Structure: Neutron Powder Diffraction Measurements," *Physical Review B* 77 (2008): 020409, https://doi.org/10.1103/PhysRevB.77.020409.

12. B. Li, X. H. Luo, H. Wang, et al., "Colossal Negative Thermal Expansion Induced by Magnetic Phase Competition on Frustrated Lattices in Laves Phase Compound (Hf,Ta) Fe_2," *Physical Review B* 93 (2016): 224405, https://doi.org/10.1103/PhysRevB.93.224405.

13. Y. Cao, K. Lin, S. Khmelevskyi, et al., "Ultrawide Temperature Range Super-Invar Behavior of $R_2(Fe,Co)_{17}$ Materials (R = Rare Earth)," *Physical Review Letters* 127 (2021): 055501, https://doi.org/10.1103/PhysRevLett.127.055501.

14. Y. Song, J. Chen, X. Liu, et al., "Zero Thermal Expansion in Magnetic and Metallic $Tb(Co,Fe)_2$ Intermetallic Compounds," *Journal of the American Chemical Society* 140 (2018): 602–605, https://doi.org/10.1021/jacs.7b12235.

15. X. Dong, K. Lin, C. Yu, et al., "Zero Thermal Expansion in Non-Stoichiometric and Single-phase $(Hf,Nb)Fe_{2.5}$ Alloy," *Scripta Materialia* 229 (2023): 115388, https://doi.org/10.1016/j.scriptamat.2023.115388.

16. S. Khmelevskyi, I. Turek, and P. Mohn, "Large Negative Magnetic Contribution to the Thermal Expansion in Iron-Platinum Alloys: Quantitative Theory of the Invar Effect," *Physical Review Letters* 91 (2003): 037201, https://doi.org/10.1103/PhysRevLett.91.037201.

17. K. Takenaka and H. Takagi, "Zero Thermal Expansion in a Pure-form Antiperovskite Manganese Nitride," *Applied Physics Letters* 94 (2009): 131904, https://doi.org/10.1063/1.3110046.

18. K. Hoshi, "Pressure Effect on the Magnetic Properties of Hf_{1-x} Ta_xFe_2," *Journal of the Physical Society of Japan* 57 (1988): 3112–3118, https://doi.org/10.1143/JPSJ.57.3112.

19. M. Azuma, W. T. Chen, H. Seki, et al., "Colossal Negative Thermal Expansion in $BiNiO_3$ Induced by Intermetallic Charge Transfer," *Nature Communications* 2 (2011): 347, https://doi.org/10.1038/ncomms1361.

20. K. Kanematsu, "Magnetic Moment in Laves Phase Compound. II. $Zr(Fe_{1-x}Mn_x)_2$ and $Zr(Fe_{1-x}Co_x)_2$," *Journal of the Physical Society of Japan* 31 (1971): 1355–1360, https://doi.org/10.1143/JPSJ.31.1355.

21. M. Jovanovic and L. M. Schoop, "Simple Chemical Rules for Predicting Band Structures of Kagome Materials," *Journal of the American Chemical Society* 144 (2022): 10978–10991, https://doi.org/10.1021/jacs.2c04183.

22. J. Xu, Z. Wang, H. Huang, et al., "Significant Zero Thermal Expansion via Enhanced Magnetoelastic Coupling in Kagome Magnets," *Advanced Materials* 35 (2023): 2208635, https://doi.org/10.1002/adma.202208635.

23. J.-X. Yin, B. Lian, and M. Z. Hasan, "Topological Kagome Magnets and Superconductors," *Nature* 612 (2022): 647–657, https://doi.org/10.1038/s41586-022-05516-0.

24. L. Ye, M. Kang, J. Liu, et al., "Massive Dirac Fermions in a Ferromagnetic Kagome Metal," *Nature* 555 (2018): 638–642, https://doi.org/10.1038/nature25987.

25. S. D. Wilson and B. R. Ortiz, "AV_3Sb_5 Kagome Superconductors," *Nature Reviews Materials* 9 (2024): 420–432, https://doi.org/10.1038/s41578-024-00677-y.

26. B. R. Ortiz, S. M. L. Teicher, Y. Hu, et al., "CsV_3Sb_5: $A\mathbb{Z}_2$ Topological Kagome Metal with a Superconducting Ground State," *Physical Review Letters* 125 (2020): 247002, https://doi.org/10.1103/PhysRevLett.125.247002.

27. L. Song, F. Zhou, H. Li, et al., "Large Anomalous Hall Effect at Room Temperature in a Fermi-Level-Tuned Kagome Antiferromagnet," *Advanced Functional Materials* 34 (2024): 2316588, https://doi.org/10.1002/adfm.202316588.

28. S. Nakatsuji, N. Kiyohara, and T. Higo, "Large Anomalous Hall Effect in a Non-Collinear Antiferromagnet at Room Temperature," *Nature* 527 (2015): 212–215, https://doi.org/10.1038/nature15723.

29. X. Song, Z. Sun, Q. Huang, et al., "Adjustable Zero Thermal Expansion in Antiperovskite Manganese Nitride," *Advanced Materials* 23 (2011): 4690–4694, https://doi.org/10.1002/adma.201102552.

30. R. Minakata, M. Shiga, and Y. Nakamura, "Spontaneous Volume Magnetostriction of RCo_2 Compounds," *Journal of the Physical Society of Japan* 41 (1976): 1435–1436, https://doi.org/10.1143/JPSJ.41.1435.

31. D. Givord and R. Lemaire, "Magnetic Transition and Anomalous Thermal Expansion in R_2Fe_{17} Compounds," *IEEE Transactions on Magnetics* 10 (2003): 109–113.

32. H. W. S. Arachchige, W. R. Meier, M. Marshall, et al., "Charge Density Wave in Kagome Lattice Intermetallic ScV_6Sn_6," *Physical Review Letters* 129 (2022): 216402, https://doi.org/10.1103/PhysRevLett.129.216402.

33. W. R. Meier, R. P. Madhogaria, S. Mozaffari, et al., "Tiny Sc Allows the Chains to Rattle: Impact of Lu and Y Doping on the Charge-Density Wave in ScV_6Sn_6," *Journal of the American Chemical Society* 145 (2023): 20943–20950, https://doi.org/10.1021/jacs.3c06394.

34. Y. Song, N. Shi, S. Deng, X. Xing, and J. Chen, "Negative Thermal Expansion in Magnetic Materials," *Progress in Materials Science* 121 (2021): 100835, https://doi.org/10.1016/j.pmatsci.2021.100835.

35. Y. Nishihara, Y. Yamaguchi, and A. Negishi, "Magneto-volume Study of the Ferro- to Antiferromagnetic Transition in $(Sc_{0.35}Ti_{0.65})Fe_2$," *Journal of Magnetism and Magnetic Materials* 54-57 (1986): 945–946, https://doi.org/10.1016/0304-8853(86)90326-4.

36. L. Sun, H. Yibole, O. Tegus, and F. Guillou, "Magnetocaloric Effect, Magnetoresistance of $Sc_{0.28}Ti_{0.72}Fe_2$, and Phase Diagrams of $Sc_{0.28}Ti_{0.72}Fe_{2-x}T_x$ Alloys with T = Mn or Co," *Crystals* 10 (2020): 410.

37. Z. Jing-Ting, H. Yibole, B. Narsu, et al., "Structural and Magnetic Properties of $Sc_{1-x}Nb_xFe_2$ Intermetallics Showing Anomalous Zero Thermal Expansion," *Intermetallics* 136 (2021): 107252, https://doi.org/10.1016/j.intermet.2021.107252.

38. Y. Song, Q. Sun, M. Xu, et al., "Negative Thermal Expansion in $(Sc,Ti)Fe_2$ Induced by an Unconventional Magnetovolume Effect," *Materials Horizons* 7 (2020): 275–281, https://doi.org/10.1039/C9MH01025D.

39. Y. Nishihara and Y. Yamaguchi, "Magnetic Properties of the $(Sc_{1-x}Ti_x)Fe_2$ System Having Two Magnetic States with Different Degrees of Localization," *Journal of the Physical Society of Japan* 55 (1986): 920–935, https://doi.org/10.1143/JPSJ.55.920.

40. M. Saoudi, J. Déportes, and B. Ouladdiaf, "Magnetic Ground state of $Ti_{1-x}Sc_xFe_2$ System," *Journal of Magnetism and Magnetic Materials* 231 (2001): 265–272.

41. W. Z. Lin, C. Yu, Q. Sun, et al., "Chemical Heterogeneity Modulated Zero Thermal Expansion Alloy Over Super-Wide Temperature Range," *Cell Reports Physical Science* 4 (2023): 101254, https://doi.org/10.1016/j.xcrp.2023.101254.

42. W. Li, K. Lin, Y. Yan, et al., "A Seawater-Corrosion-Resistant and Isotropic Zero Thermal Expansion $(Zr,Ta)(Fe,Co)_2$ Alloy," *Advanced Materials* 34 (2022): 2109592, https://doi.org/10.1002/adma.202109592.

43. C. Yu, K. Lin, X. Chen, et al., "Superior Zero Thermal Expansion Dual-Phase Alloy via Boron-Migration Mediated Solid-State Reaction," *Nature Communications* 14 (2023): 3135, https://doi.org/10.1038/s41467-023-38929-0.

44. Y. Cao, Y. Xu, S. Khmelevskyi, et al., "Interplanar Magnetic Orders and Symmetry-Tuned Zero Thermal Expansion in Kagomé Metal $(Zr,Ta)Fe_2$," *Chemistry of Materials* 35 (2023): 9167–9174, https://doi.org/10.1021/acs.chemmater.3c01894.

45. M. Shiga and Y. Nakamura, "Magnetovolume Effects and Invar Characters of $(Zr_{1-x}Nb_x)Fe_2$," *Journal of the Physical Society*

of Japan 47 (1979): 1446–1451, https://doi.org/10.1143/JPSJ.47.1446.

46. Y. Song, Q. Sun, T. Yokoyama, et al., "Transforming Thermal Expansion from Positive to Negative: the Case of Cubic Magnetic Compounds of $(Zr,Nb)Fe_2$," *The Journal of Physical Chemistry Letters* 11 (2020): 1954–1961, https://doi.org/10.1021/acs.jpclett.9b03880.

47. A. E. Phillips, G. J. Halder, K. W. Chapman, A. L. Goodwin, and C. J. Kepert, "Zero Thermal Expansion in a Flexible, Stable Framework: Tetramethylammonium Copper(I) Zinc(II) Cyanide," *Journal of the American Chemical Society* 132 (2010): 10–11, https://doi.org/10.1021/ja906895j.

48. Y. Sun, R. Yu, S. Khmelevskyi, et al., "Local Chemical Heterogeneity Enabled Superior Zero Thermal Expansion in Nonstoichiometric Pyrochlore Magnets," *National Science Review* 12 (2025): nwae462, https://doi.org/10.1093/nsr/nwae462.

49. J. P. Perdew, K. Burke, and M. Ernzerhof, "Generalized Gradient Approximation Made Simple," *Physical Review Letters* 77 (1996): 3865, https://doi.org/10.1103/PhysRevLett.77.3865.

50. S. Khmelevskyi and S. Steiner, "Predictive Theory of Anomalous Volume Magnetostriction in Fe–Ni Alloys: Bond Repopulation Mechanism of the Invar Effect," *The Journal of Physical Chemistry C* 128 (2023): 605–612, https://doi.org/10.1021/acs.jpcc.3c07037.

51. B. L. Gyorffy, "Coherent-Potential Approximation for a Nonoverlapping-Muffin-Tin-Potential Model of Random Substitutional Alloys," *Physical Review B* 5 (1972): 2382, https://doi.org/10.1103/PhysRevB.5.2382.

52. I. Abrikosov and H. L. Skriver, "Self-Consistent Linear-muffin-Tin-Orbitals Coherent-Potential Technique for Bulk and Surface Calculations: Cu-Ni, Ag-Pd, and Au-Pt Random Alloys," *Physical Review B* 47 (1993): 16532, https://doi.org/10.1103/PhysRevB.47.16532.

53. B. Gyorffy, A. Pindor, J. Staunton, G. Stocks, and H. Winter, "A First-Principles Theory of Ferromagnetic Phase Transitions in Metals," *Journal of Physics F: Metal Physics* 15 (1985): 1337, https://doi.org/10.1088/0305-4608/15/6/018.

54. A. I. Liechtenstein, M. Katsnelson, V. Antropov, and V. Gubanov, "Local Spin Density Functional Approach to the Theory of Exchange Interactions in Ferromagnetic Metals and Alloys," *Journal of Magnetism and Magnetic Materials* 67 (1987): 65–74.

55. A. V. Ruban, S. Simak, S. Shallcross, and H. L. Skriver, "Local Lattice Relaxations in Random Metallic Alloys: Effective Tetrahedron Model and Supercell Approach," *Physical Review B* 67 (2003): 214302, https://doi.org/10.1103/PhysRevB.67.214302.

Supporting Information

Additional supporting information can be found online in the Supporting Information section.

Supporting File: smll72494-sup-0001-SuppMat.docx.